Integrated all-Si traveling-wave optical modulators and photodetectors operating beyond 40 GHz

Shao-Ming Wu,[a] Yun-Teng Shih,[a] Wen-Chi Tsai,[a] Jian-Jer Tang,[a] and Ming-Chang M. Lee[a,b,*]

[a]National Tsing Hua University, Institute of Photonics Technologies, Hsinchu, Taiwan
[b]National Tsing Hua University, Department of Electrical Engineering, Hsinchu, Taiwan

Abstract. We present high-speed, traveling-wave (TW) Si Mach–Zehnder modulators and Si sub-bandgap photodetectors (SBPD) monolithically integrated on an Si-only photonics platform without incorporation of Ge epitaxial growth process. Through constructing a detailed equivalent circuit model on the components, we design the device structure and TW electrodes for operating the device with bandwidth beyond 40 GHz. The experimental results show the 3-dB bandwidths of the Si modulator and photodetectors are 35 and 44 GHz, respectively, generally agreeing well with our design. The measured photoresponsivity of the SBPD varies from 0.1 A/W to nearly 1 A/W, depending on the bias voltage. These two components potentially can be utilized for an integrated optical transceiver operating for 50 Gbit/s data transmission. [DOI: 10.1117/1.JOM.1.1.014002]

Keywords: Si photonics; high-speed modulator; high-speed photodetector; optical transceiver.

Paper 20013 received Sep. 24, 2020; accepted for publication Jan. 5, 2021; published online Jan. 26, 2021.

1 Introduction

With the advent of 5G mobile network in recent years, the demand for high-speed data transmission has increased significantly. Optical transmission in general is superior to electrical transmission in terms of wide transmission bandwidth, long distance, low latency, and low energy consumption. Recently high-speed integrated optical transceivers implemented via silicon photonics technology have received considerable attention. About 400 Gb/s multi-channel Si photonics optical transceivers utilized in data centers have been demonstrated in 2019.[1] All the passive and active optical components are monolithically integrated on a single chip and are fabricated through a CMOS-compatible process.

To implement a complete optical function on a Si photonics chip, several key optical components are required, including lasers, modulators,[2] photodetectors,[3] multiplexers/demultiplexers,[4,5] and filters. Among these components, lasers made of III–V semiconductor compound are usually demanded. They are either packaged[6] or bonded and then processed[7] on as-patterned Si structures to make light sources since Si is an indirect bandgap semiconductor with low radiation efficiency. In addition, photodetector is another component that requires different materials for detecting optical signals and then converting into electrical. Ge is commonly utilized as the photodetector material for Si photonics. Although heterogeneous epitaxy of Ge on Si has made great progress, the process condition is still critical and difficult to be controlled. In this research, we are interested in using defect-mediated Si sub-bandgap photodetectors (SBPD) to detect optical signals on Si photonic devices. Si SBPD have been previously reported for implementing transparent waveguide power monitors.[8] With this device, all the components, except the light source, can be accomplished by pure Si structures via a simpler fabrication process. However, optical absorption of the defect-mediated Si SBPD is generally weak, and therefore it needs a long waveguide structure or a ring resonator[9] to enhance the responsivity. Nevertheless, long devices are easy to create a problem of low operating speed because of a large device resistor-capacitor (RC) time constant. To improve the operating speed, a traveling-wave (TW) type

*Address all correspondence to Ming-Chang M. Lee, mclee@ee.nthu.edu.tw

waveguide photodetector is desirable. Although a TW Si SBPD was presented before Ref. 10, it lacked device design and analysis. In this research, we build up a detailed equivalent circuit model to analyze device bandwidth on a Si TW Mach–Zehnder modulator (TW-MZM) and a Si TW SBPD (TW-SBPD). By integrating both components on the same chip, we demonstrate an integrated all-Si optical transceiver.

2 Design and Analysis of Si Traveling-wave MZM and SBPD

This section focuses on design and modeling of the Si TW-MZM and the Si TW-SBPD. Figure 1 shows the device cross section. The Si TW-MZM is based on a waveguide phase shifter implemented by an L-shape PN junction while the Si TW-SBPD is a waveguide PIN junction implanted with Si ions to introduce deep trapped states inside. Both the Si TW-MZM and TW-SBPD are interconnected by Si rib waveguides, and light in the waveguides is coupled to fibers through grating couplers. The Si TW-MZM and TW-SBPD are analyzed via a modified equivalent circuit model referred in paper[11] with key device parameters calculated by Synopsys Sentaurus TCAD.

2.1 *Si Traveling-Wave MZM*

The Si MZM is configured with an asymmetric waveguide-based Mach–Zehnder interferometer with a phase shifter at either arm of the device. The modulation mechanism of phase shift is through the plasma dispersion effect in silicon, by controlling the charge density inside the Si waveguide. The charge density is manipulated by either injecting or depleting carriers on an embedded PN junction so as to convert the electrical signal into a modulated optical signal. Because the plasma dispersion effect is weak, a high-speed Si MZM usually needs a TW design to achieve a large enough modulation depth.

The cross section of the waveguide phase shifter for the Si TW-MZM is shown in Fig. 2. The Si rib waveguide is 400-nm wide and 220-nm high with a slab thickness of 70 nm. The operating wavelength is targeted at 1310 nm. Inside the waveguide, an L-shape PN junction with a dopant

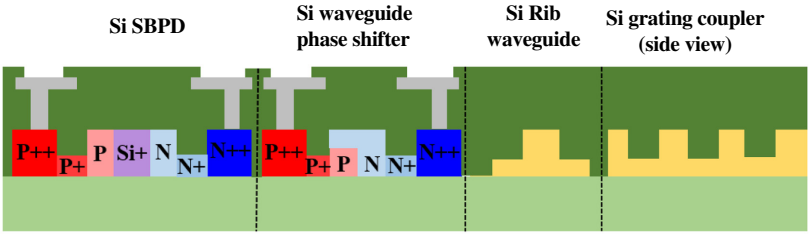

Fig. 1 Schematic illustration of the components in cross section: Si SBPD, Si waveguide phase shifter, Si rib waveguide, and Si grating coupler.

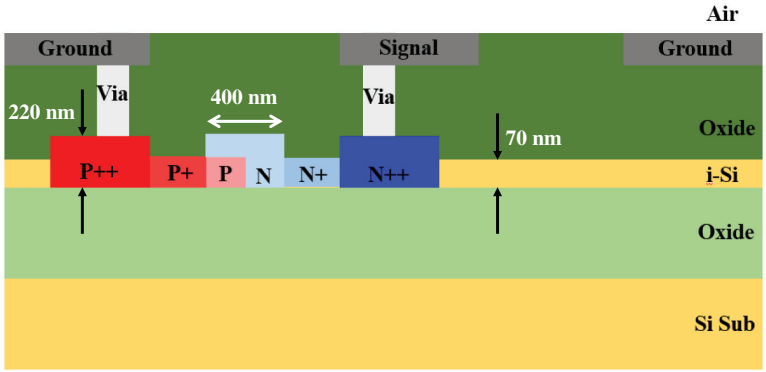

Fig. 2 Cross section of the waveguide phase shifter in the Si TW-MZM.

concentration P-type (5e17 cm^{-3}) and N-type (1e18 cm^{-3}) is formed at the center of waveguide core. Outside the core region are medium doped (P+, N+) waveguide slabs extended to the heavily doped regions (P++, N++), which directly contact the TW electrodes via holes. The TW electrodes are featured as a coplanar waveguide (CPW) transmission line, where the signal is applied on the N-type Si.

The operating speed of a Si TW-MZM is determined by three factors: (1) the characteristic impedance of transmission line, (2) the velocity mismatch between the microwave and the optical wave, and (3) the attenuation coefficient of transmission line. The basic idea to analyze the CPW transmission line is to establish its equivalent circuit model under the quasi-TEM approximation.[11] We first calculate the partial capacitance[12] of each layer by the conformal mapping technique[13] and then simulate the junction capacitance and series resistance of the L-shape PN junction. All these component parameters are used for constructing the CPW equivalent circuit model. The equivalent circuit model of the loaded CPW with respect to the component structure is shown in Fig. 3.

We first specify each layered partial capacitance imposed on the TW electrode,[11] and calculate the value by considering the type of dielectric material, layer structure, electrode dimension, and the gap between electrodes. After we find the junction capacitance C_{pn} and the series resistance Z_s of the L-shape PN junction and the CPW inductance L and resistance R, we can construct a complete equivalent circuit of the loaded CPW shown in Fig. 4.

The junction capacitance C_{pn} and the series resistance Z_S of the L-shape PN junction are obtained by a simulation tool (Sentaurus TCAD, Synopsys). We first establish the model and verify the dopant concentration and electric field shown in Fig. 5. Frequency-dependent C_{pn} and Z_S are then extracted by examining the simulated small-signal I–V characteristics of the junction. The transmission line inductance can be decomposed into the external and internal

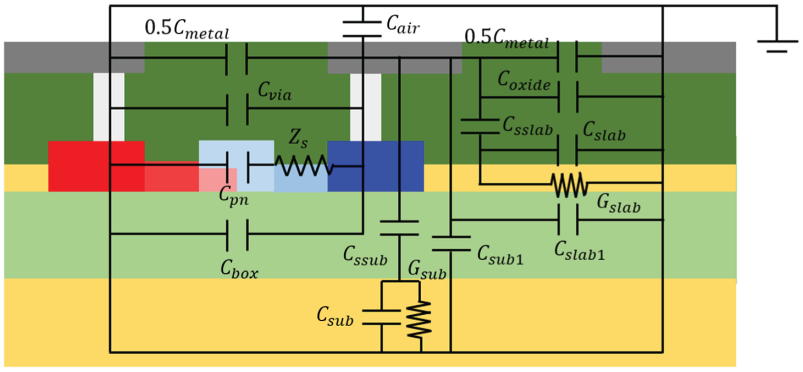

Fig. 3 Illustration of the equivalent circuit model of the TW waveguide phase shifter.

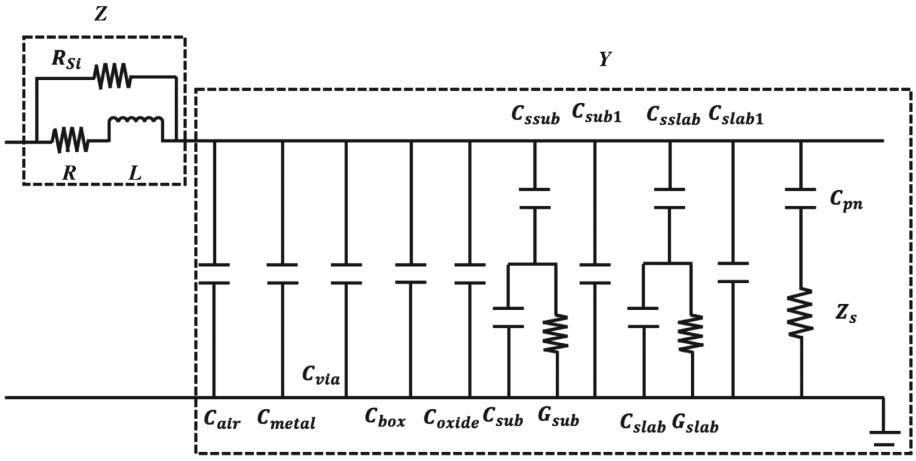

Fig. 4 Schematics of the loaded transmission line model of the waveguide phase shifter.

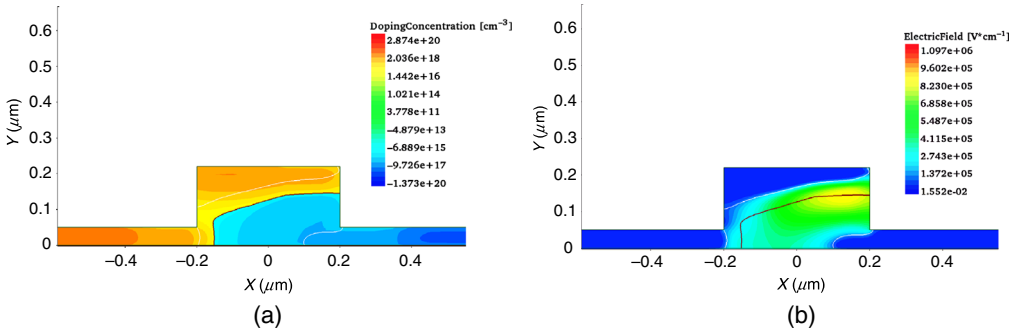

Fig. 5 Simulation results on the L-shape PN junction: (a) the dopant concentration and (b) the electric field (at 0 V).

Table 1 The equivalent transmission line parameters.

R_{eff}	L_{eff}	G_{eff}	C_{eff}
1.0865×10^4 Ω/m	4.9495×10^{-7} H/m	20.4112 Ω^{-1}/m	2.3595×10^{-10} F/m

one. The former is independent of frequency, which can be obtained by considering the same CPW structure in the air; the latter is frequency-dependent, which can be calculated by Wheeler's incremental inductance rule.[14] In fact, the microwave also propagates in the Si substrate. However, because the silicon resistance is much higher than that of metal line, the shunt resistance R_{Si} generally can be ignored. By taking all the electrical elements into account, we can derive the parametric resistance R_{eff}, inductance L_{eff}, conductance G_{eff}, and capacitance C_{eff} of a general transmission-line circuit model. The values are listed in Table 1.

With knowing the transmission line parameters, we are able to find the characteristic impedance, phase constant and attenuation coefficient of the loaded transmission line. We therefore analyze the operating speed of the TW modulator by examining the frequency response of the normalized average voltage across the depletion region of the L-shape PN junction, which is given as[11]

$$m(\omega_m) = \left| \frac{V_{dep}(\omega_m)}{V_{dep}(\omega_0)} \right| = \left| \frac{(1 + j\omega_0 C_{pn} Z_s) V_{avg}(\omega_m)}{(1 + j\omega_m C_{pn} Z_s) V_{avg}(\omega_0)} \right|, \tag{1}$$

where V_{dep} is the average voltage across the depletion region, ω_m and ω_0 represent the operating radio frequency and the frequency near DC, respectively, and V_{avg} is the average voltage across the transmission line. In fact, the amplitude of the TW voltage should vary along the transmission line. Nevertheless, we can expect that the overall phase change is proportional to the average voltage across the transmission line multiplied with the length. According to the transmission line theory, we can derive the average voltage given as

$$V_{avg}(\omega_m) = \frac{V_g(1 + \rho_1)e^{i\beta_0 l}}{2[e^{\gamma l} + \rho_1 \rho_2]e^{-\gamma l}} (V_+ + \rho_2 V_-), \tag{2}$$

where V_g is the input voltage, β_0 is the optical propagation constant, γ is the complex microwave propagation constant, l is the length of transmission line, and V_+ and V_- are the forward and backward TW voltages on the transmission line. $\rho_1 = \frac{Z_0 - Z_s}{Z_0 + Z_s}$ and $\rho_2 = \frac{Z_L - Z_0}{Z_L + Z_0}$, which are the reflection coefficients at the input and output ends. Z_0 is the characteristic impedance of the transmission line, and Z_S and Z_L are the source and load impedances, respectively.

Equations (1) and (2) already imply that the frequency response of the TW modulator is influenced by the impedance mismatch, microwave loss, RC time constant of the PN junction, and phase velocity mismatch of the optical wave and microwave. According to our designed Si

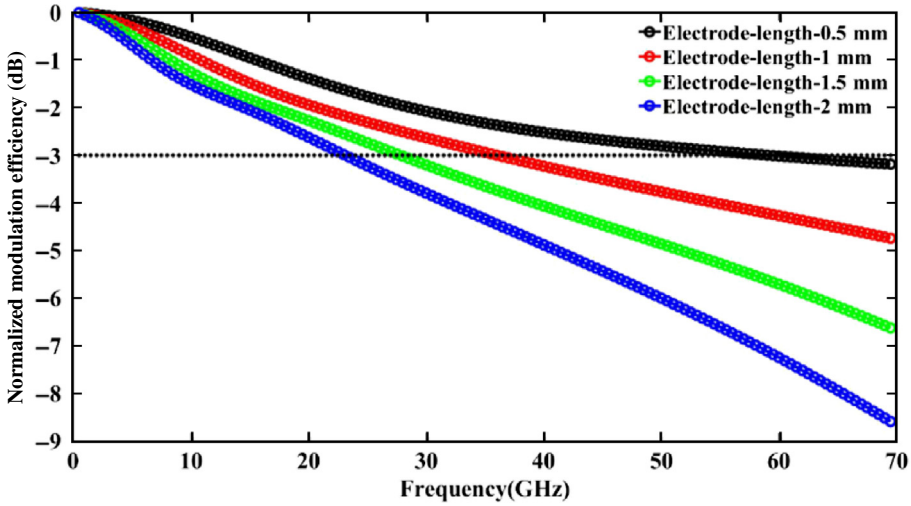

Fig. 6 Simulated frequency response of the normalized modulation efficiency of the Si TW-MZM with respect to different electrode lengths.

waveguide and CPW structures, under the assumption of impedance match condition, we plot the frequency response of modulation efficiency of Si TW-MZM for different lengths, from 0.5 to 2 mm, as shown in Fig. 6. The 3-dB bandwidth apparently decreases with the electrode length due to the microwave loss. However, a longer electrode length is better for higher modulation efficiency.

2.2 *Si Traveling-Wave SBPD*

Silicon intrinsically is transparent for radiation spectrum beyond 1130 nm in wavelength. To generate photoresponse at communication bands (for example, 1310 or 1550 nm), one way to do it is through defect-mediated sub-bandgap absorption. Via the deep-level charge states within the silicon bandgap, sub-bandgap photons could be absorbed and initiate an optical transition of electrons from the valence band to the conduction band. Figure 7 shows the mechanism of the optical transition. The deep-level charge states have an energy level below the conduction band by E_{dl}, which enables electrons to be excited from the valence band to the deep-level states by absorbing photons with energy $\mathrm{hv} > E_g - E_{dl}$. The electrons will be subsequently transferred to the conduction band through thermal excitation. The basic idea is similar to a reverse process of Shockley–Read–Hall recombination. The sub-bandgap absorption efficiency depends on the type and density of the deep-level states. More details about the model and analysis of defect-mediated sub-bandgap absorption can be found in Ref. 15.

In general, the optical transition through sub-bandgap absorption is relatively weak. To enhance photoresponsivity, long and ion-implanted silicon waveguide photodetectors are

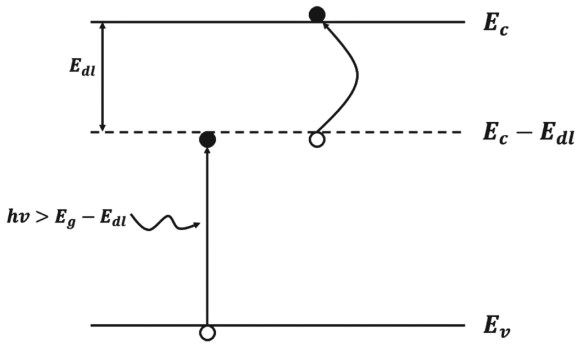

Fig. 7 Illustration of defect-mediated sub-bandgap absorption.

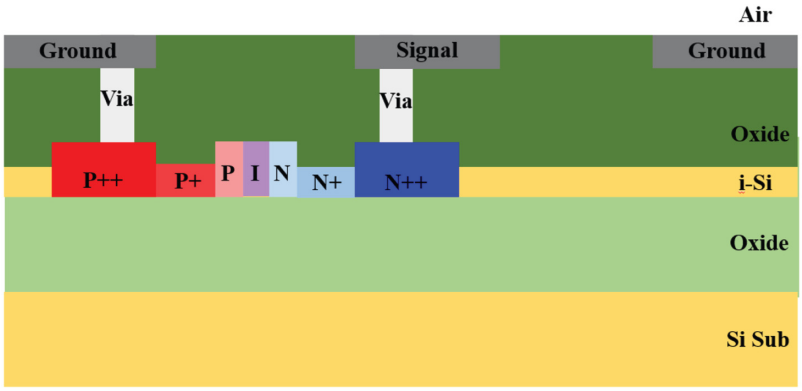

Fig. 8 Cross section of the Si TW-SBPD.

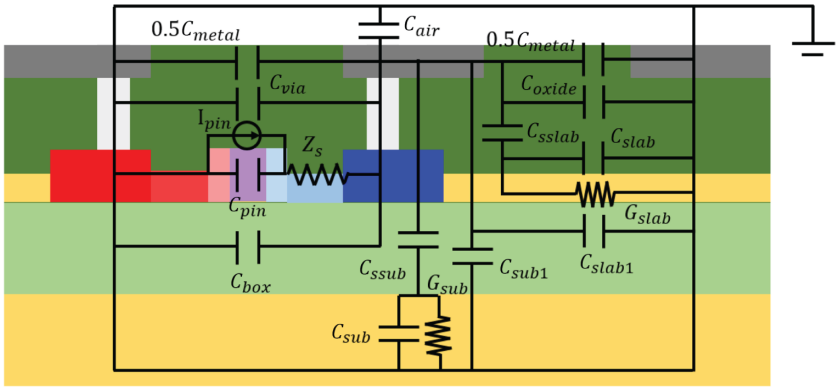

Fig. 9 Illustration of the equivalent circuit model of the Si TW-SBPD.

employed to have a larger responsivity.[16] Nevertheless, the waveguide absorption length is still required to be several millimeters long. Such a long waveguide photodetector could have limitation on the operating speed. A TW photodetector design is desired to improve the speed. In this study, we optimize the waveguide structure and the TW electrode to implement a high-speed Si TW-SBPD.

The device structure is shown in Fig. 8. Unlike the Si MZM, a lateral PIN junction is employed on the waveguide core of the photodetector, where the intrinsic region is implanted with Si+ ions to enhance sub-bandgap absorption. Meanwhile, the waveguide width is extended to 800 nm to have a larger absorption region. A CPW design is also applied for this TW photodetector.

The Si TW-SBPD speed is determined by the internal photocarrier transit time and all the other parameters of the transmission line discussed in the previous section. The corresponding equivalent circuit model of the TW-SBPD is shown in Fig. 9. It is similar to the Si TW-MZM except for a current source across the PIN to represent the photo-generated current. Therefore, the analysis of the TW-SBPD is slightly different from the way we analyze TW-MZM. Here, we use the telegrapher's equation[17] and the approach to calculate the transmission line parameters in the previous section to investigate the frequency response of the photodetector.

We replot the equivalent transmission line model of the TW-SBPD shown in Fig. 10. The current source shown in this model is expressed as[17]

$$\frac{dI_{pin}(z)}{dz} = k_0 e^{-\gamma_0 z}, \tag{3}$$

where $k_0 = \frac{4\alpha_0 \xi e P_0 \lambda_0}{hc}$, ξ is the intrinsic quantum efficiency, e is the electron charge, h is Planck's constant, c is the speed of light in vacuum, P_0 is the input waveguide power, λ_0 is wavelength,

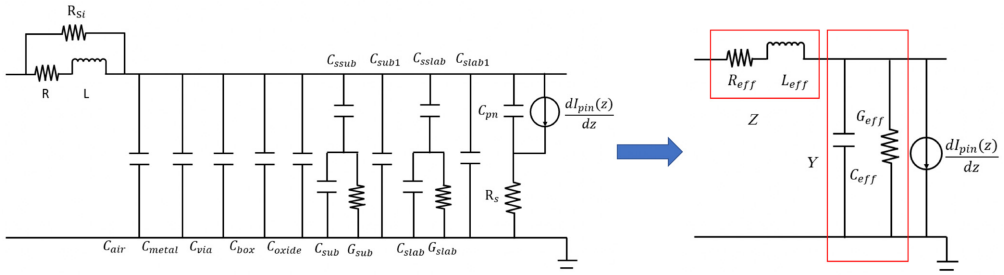

Fig. 10 Schematics of the loaded transmission line model of the Si TW-SBPD.

γ_0 is the complex propagation constant of modulated optical wave, α_0 is the absorption coefficient of optical wave, and z is the distance from the TW-SBPD input end. Next, we consider drift and diffusion of the photo-generated carriers and rewrite the express of the current source as

$$\frac{dI'_{pin}(z)}{dz} = \frac{dI_{pin}(z)}{dz}\frac{1}{1+j\frac{\omega}{\omega_c}}\left[\frac{A_{drift}}{1+j\omega\tau_{drift}} + \frac{A_{diff}}{1+j\omega\tau_{diff}}\right], \tag{4}$$

where I'_{pin} is a modified expression of I_{pin} from the transmission line model shown in Fig. 10, ω is frequency, ω_c is the RC time constant associated with C_{pin} and R_s, A_{drift} and A_{diff} are the ratios of photocurrent contributed by drift and diffusion of the photo-generated carriers, respectively, and τ_{drift} and τ_{diff} are the corresponding time constants. The junction capacitance C_{pin} and the series resistance R_s of the PIN junction are obtained by simulation (Sentaurus TCAD, Synopsys). The simulated depletion region of the PIN junction is shown in Fig. 11.

According to the equivalent transmission line model shown in Fig. 10, we can modify the telegrapher's equation with the current source, which is given as

$$\begin{cases} \dfrac{dV(z)}{dz} = -ZI(z) \\ \dfrac{dI(z)}{dz} = -YV(z) - \dfrac{dI'_{pin}(z)}{dz} \end{cases}, \tag{5}$$

where Z is the transmission line impedance and Y is the admittance. After combing these two equations, we can write down a second order differential equation below:

$$\frac{d^2V}{d^2z} - \gamma_e^2 V = Zk_0 e^{-\gamma_0 z}, \tag{6}$$

where $\gamma_e = \sqrt{ZY}$ is the complex microwave propagation constant. If we assuem the input end of the TW electrode is open and the output end is connected to a load, i.e, $I(0) = 0$, $\frac{V(l)}{I(l)} = Z_l$,

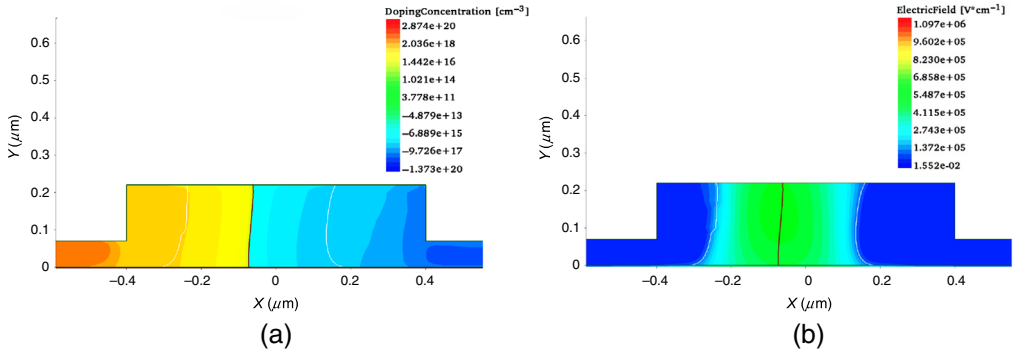

Fig. 11 Simulation results on the Si TW-SBPD: (a) the dopant concentration and (b) the electric field (at 0 V).

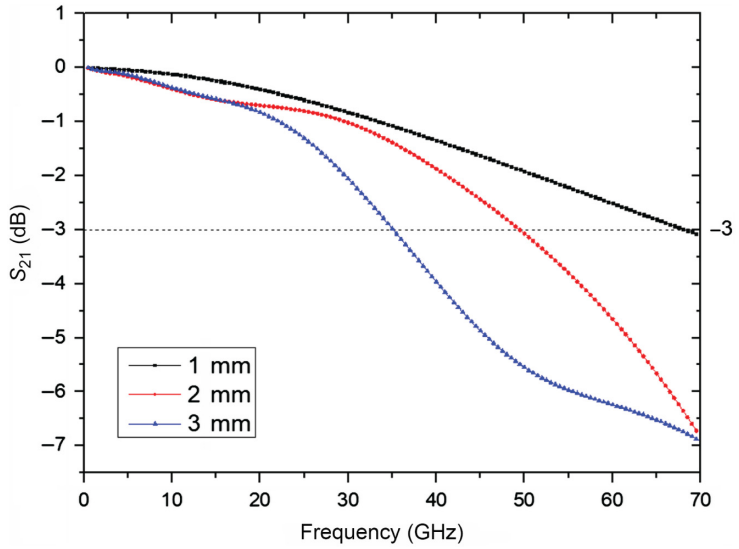

Fig. 12 Simulated frequency response of the normalized responsivity of the Si TW-SBPD with respect to different waveguide absorption lengths.

where Z_l is the impedance of the load, we can write down the TW signal on the transmission line with an expression of

$$V(z) = V_1 e^{\gamma_e z} + V_2 e^{-\gamma_e z} + \frac{Zk_0}{(\gamma_o^2 - \gamma_e^2)} e^{-\gamma_0 z}, \tag{7}$$

where the first term represents the forward traveling wave, the second term is the backward traveling wave, and the last term represent the signal generated by the distributed current source at distance z. The details of V_1 and V_2 are given as

$$\begin{cases} V_1 = \frac{k_0[\gamma_e(Z_l\gamma_o - Z)e^{-\gamma_o l} - \gamma_o(Z_l\gamma_e - Z)e^{-\gamma_e l}]}{\gamma_e(\gamma_o^2 - \gamma_e^2)\left[\left(1 - \frac{Z_l}{Z_o}\right)e^{-\gamma_e l} + \left(1 + \frac{Z_l}{Z_o}\right)e^{\gamma_e l}\right]} \\ V_2 = \frac{k_0[\gamma_e(Z_l\gamma_o - Z)e^{-\gamma_o l} - \gamma_o(Z_l\gamma_e + Z)e^{\gamma_e l}]}{\gamma_e(\gamma_o^2 - \gamma_e^2)\left[\left(1 - \frac{Z_l}{Z_o}\right)e^{-\gamma_e l} + \left(1 + \frac{Z_l}{Z_o}\right)e^{\gamma_e l}\right]} \end{cases}, \tag{8}$$

where Z_o is the characteristic impedance of the loaded transmission line.

According to the equivalent circuit model and Eqs. (7) and (8), we analyze the frequency response of the TW photodetector. Here, we assume the sub-bandgap absorption coefficient is 10 dB/cm (according to the measured responsivity in the following section) and the load impedance is 50 Ω without considering the diffusion current. We obtain the frequency responses for the waveguide absorption length equal to 1, 2, and 3 mm. The results are shown in Fig. 12. In general, a longer waveguide length is better for high responsivity while the operating speed decreases due to the transmission line loss. For our fabricated device, the waveguide length is designed to be 2 mm.

3 Experimental Results and Measurement

The device is fabricated in Taiwan Semiconductor Research Institute via a self-developed Si photonics fabrication process. Si multiplexer/demultiplexers, grating couplers, TW-MZM, and TW-SBPD are all integrated together to implement a chip-scale optical transceiver. The fabricated devices are shown in Fig. 13. Single-mode fibers are coupled to the Si waveguides through the grating couplers. To test high-frequency performance of the components, we prepare two experimental configurations using a vector network analyzer to examine the optical-electrical S-parameters, as shown in Fig. 14. The device is designed for the operating wavelength in O-band (1260 to 1360 nm). To compensate the coupling loss from gratings, before the light

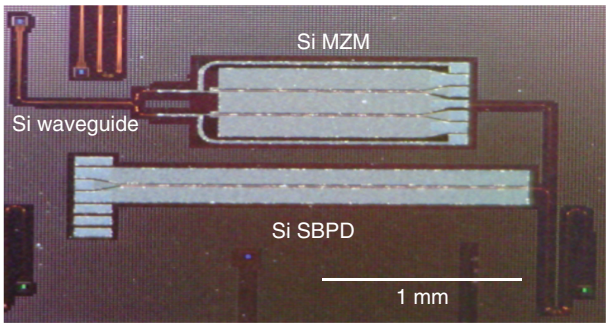

Fig. 13 Optical image of fabricated devices.

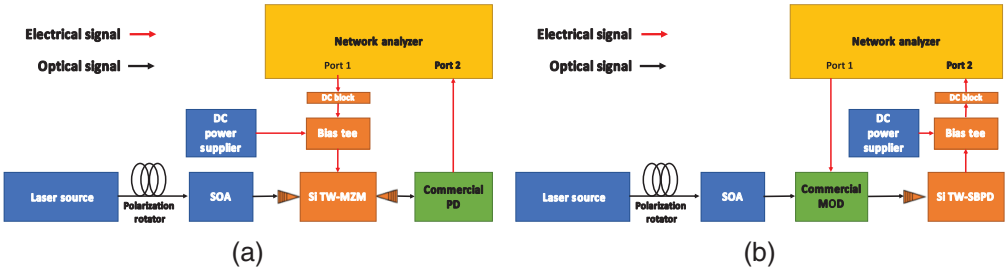

Fig. 14 Experimental setup to measure the frequency response of (a) Si TW-MZM and (b) Si TW-SBPD.

coupled to the waveguide, we use a semiconductor optical amplifier to boost the signal power to be around 20 mW and control the polarization parallel to the grating. Because both the Si TW-MZM and TW-SBPD require DC bias to optimize the operating condition, we use bias tee to mix the DC and radio frequency (RF) signal and feed it into the devices.

3.1 *Si Traveling-Wave MZM*

We test an asymmetric Si TW-MZM with an electrode length of 1 mm. We first investigate the modulation efficiency by examining the spectral shift of device transmittance versus the applied voltage. The bias-dependent spectral shift is then converted into phase change of the waveguide phase shifter. The modulation efficiency, characterized by $V\pi \cdot L$, is calculated and shown in Fig. 15. We can find that between 2 and 5 V, the modulation efficiency is nearly a constant around 1.9 V cm.

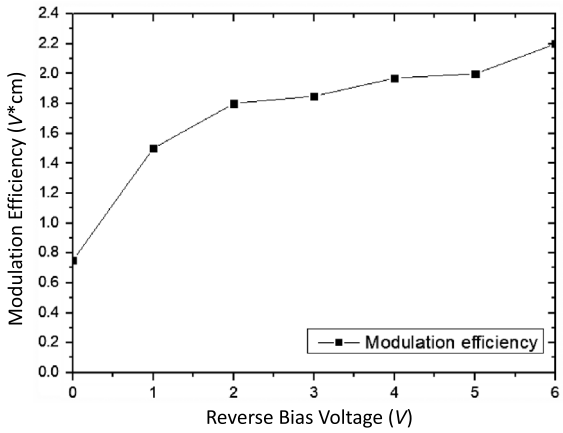

Fig. 15 Measured modulation efficiency of the Si TW-MZM at different bias voltages.

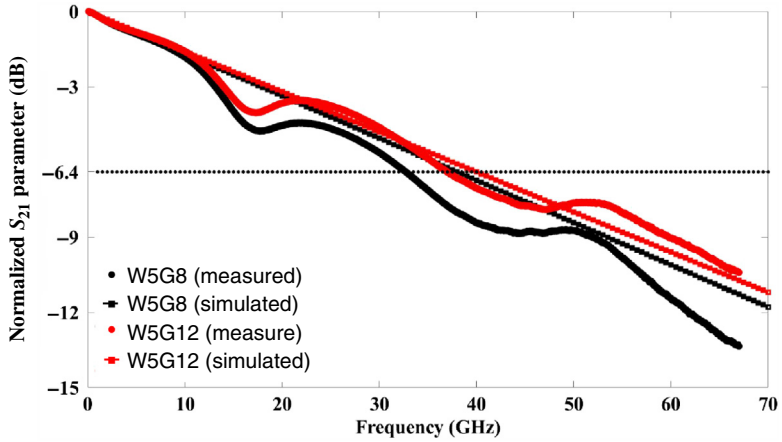

Fig. 16 Simulated and measured S_{21} parameters of the Si TW-MZM.

The simulated and measured electrical S_{21} parameters for the modulators with different CPW gaps between the ground and signal ($G = 8$ and 12 μm) at 4-V bias are shown in Fig. 16. The CPW width is 5 μm. The simulated and measured S parameters generally agree well with each other. To investigate the frequency response of the modulator, we measure the characteristic impedance of the load CPW transmission line and find the value to be around 40 to 50 Ω, which is very close to the load impedance 50 Ω. According to Eqs. (1) and (2), we thus estimate the 3-dB bandwidth of the modulator, which is corresponding to the measured 6.4-dB bandwidth of the electrical S_{21} parameter,[18] to be around 35 to 40 GHz.

3.2 *Si Traveling-Wave SBPD*

First, we investigate the photoresponsivity of the Si SBPD. Figure 17 shows the IV curves with respect to different input waveguide powers. The black line is the dark current, which is <10 nA as the bias voltage is lower than 15 V. The dark current increases prominently near 25 V, where avalanche breakdown begins to emerge. The photocurrent is proportional to the optical power and also increases with the bias voltage. According to the measured IV curves, we estimate the responsivity of the Si SBPD varied by voltage, which is given in Fig. 18. The responsivity is around 0.2 A/W as the bias voltage is lower than 20 V, and it increase significantly toward the device breakdown. The responsivity exceeds 1 A/W as the bias voltage is over 24.5 V.

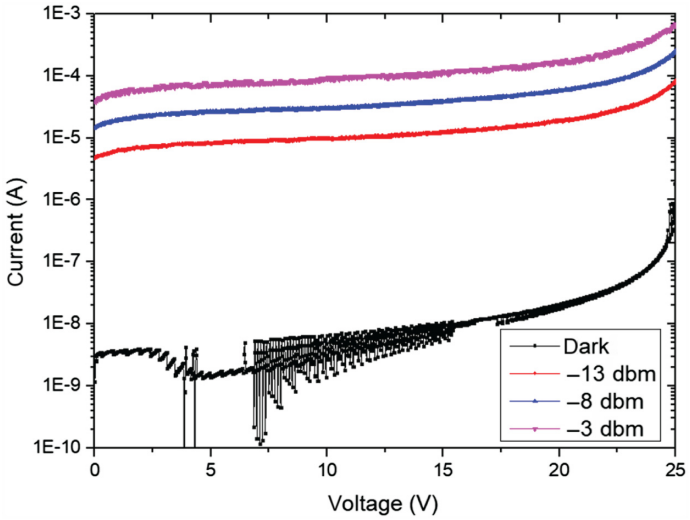

Fig. 17 Measured IV curves of the Si TW-SBPD with respect to different waveguide powers.

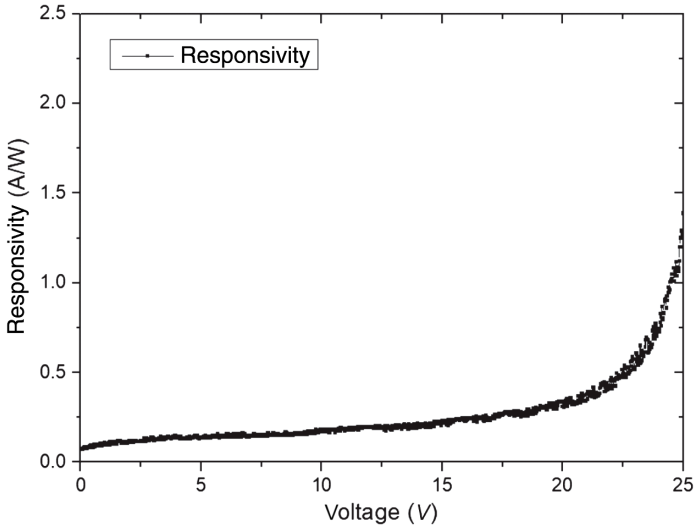

Fig. 18 Measured responsivity of the Si TW-SBPD varied by bias voltage.

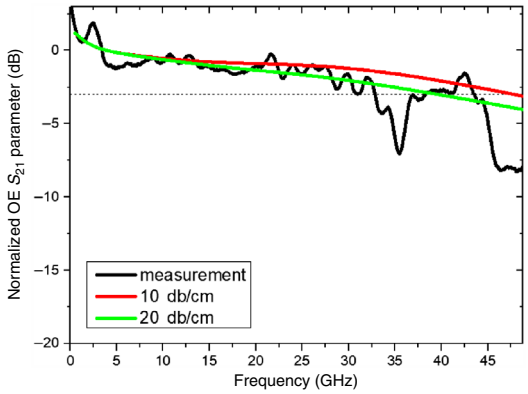

Fig. 19 Simulated and measured S_{21} parameters of the Si TW-SBPD.

The high-frequency response of the Si TW-SBPD is evaluated by examining the optical-to-electrical (OE) S_{21} parameter. We first generate a modulated optical signal via a commercial MZM. This optical signal is then coupled to the Si TW-SBPD biased at a voltage of 23 V. Figure 19 shows the measured OE S_{21} parameter. From 0 to 5 GHz, there is a jump of response, which is attributed to the diffusion current generated in the waveguide core with low electric field. In addition, near 35 GHz, there is a dip of response, which is caused by a non-ideal metal contact of the RF probe on the electrode pad. Since it is difficult to accurately distinguish the diffusion current and the drift current from measurement, we consider the diffusion current term [Eq. (4)] in our simulation model and fit it into the experimental result to plot two curves shown in Fig. 19. The red curve is for waveguide absorption coefficient 10 dB/cm and the green curve is for 20 dB/cm. The diffusion time constant is estimated to be 88 ps. The green curve is better fit with the measured data. In fact, the 20 dB/cm absorption coefficient also approximates to the measured responsivity shown in Fig. 18. By excluding the diffusion current, the 3-dB bandwidth is estimated to be 44 GHz.

4 Conclusion

We present an all-Si photonics platform with Si TW-MZM and Si TW-SBPD to realize high-speed optical transceivers. Both components are TW devices for high-frequency operation. Through a detailed design and modeling on the device configuration, both components can

operate beyond 40 GHz, which are applicable for 50 Gbit/s data transmission. The measured modulation efficiency and operating bandwidth of the Si TW-MZM are 1.9 V? cm and 35 GHz, respectively. The photoresponsivity of the Si TW-SBPD is around 0.2 A/W as the bias voltage is lower than 20 V and exceeds 1 A/W when the voltage is over 24.5 V. The operating bandwidth of the Si TW-SBPD is measured to be 44 GHz. Compared with common Ge photodetectors, Si TW-SBPD can be implemented by a simpler Si fabrication process and applied for transparent waveguide power monitors. On the other hand, because of a relatively small absorption coefficient, the Si TW-SBPD potentially is able to detect high-power optical signal but still keeps good linearity.

Acknowledgments

This research work is funded by Ministry of Science and Technology under grant No. 109-2224-E-007-001- in Taiwan.

References

1. F. Boeuf et al., "A silicon photonics technology for 400 Gbit/s applications," in *IEEE Int. Electron Devices Meeting* (2019).
2. M. Streshinsky et al., "Low power 50 Gb/s silicon traveling wave Mach–Zehnder modulator near 1300 nm," *Opt. Express* **21**(25), 30350–30357 (2013).
3. H. Chen et al., "−1 V bias 67 GHz bandwidth Si-contacted germanium waveguide p-i-n photodetector for optical links at 56 Gbps and beyond," *Opt. Express* **24**(5), 4622–4631 (2016).
4. F. Horst et al., "Cascaded Mach–Zehnder wavelength filters in silicon photonics for low loss and flat pass-band WDM (de-) multiplexing," *Opt. Express* **21**(10), 11652–11658 (2013).
5. R. J. Lycett, D. F. G. Gallagher, and V. J. Brulis, "Perfect chirped Echelle grating wavelength multiplexor: design and optimization," *IEEE Photonics J.* **5**(2), 2400123–2400123 (2013).
6. L. Carroll et al., "Photonic packaging: transforming silicon photonic integrated circuits into photonic devices," *Appl. Sci.* **6**(12), 426 (2016).
7. J. M. Ramirez et al., "III–V-on-silicon integration: from hybrid devices to heterogeneous photonic integrated circuits," *IEEE J. Sel. Top. Quantum Electron.* **26**(2), 1–13 (2020).
8. T. Baehr-Jones, M. Hochberg, and A. Scherer, "Photodetection in silicon beyond the band edge with surface states," *Opt. Express* **16**(3), 1659–1668 (2008).
9. J. K. Doylend, P. E. Jessop, and A. P. Knights, "Silicon photonic resonator-enhanced defect-mediated photodiode for sub-bandgap detection," *Opt. Express* **18**(14), 14671–14678 (2010).
10. H. Zhu, K. Goi, and K. Ogawa, "All-silicon waveguide photodetection for low-bias power monitoring and 20-km 28-Gb/s NRZ-OOK signal transmission," *IEEE J. Sel. Top. Quantum Electron.* **24**(2), 1–7 (2018).
11. H. Yu and W. Bogaerts, "An equivalent circuit model of the traveling wave electrode for carrier-depletion-based silicon optical modulators," *J. Lightwave Technol.* **30**(11), 1602–1609 (2012).
12. E. Chen and S. Y. Chou, "Characteristics of coplanar transmission lines on multilayer substrates: modeling and experiments," *IEEE Trans. Microwave Theory Tech.* **45**(6), 939–945 (1997).
13. E. Carlsson and S. Gevorgian, "Conformal mapping of the field and charge distributions in multilayered substrate CPWs," *IEEE Trans. Microwave Theory Tech.* **47**(8), 1544–1552 (1999).
14. W. Heinrich, "Quasi-TEM description of MMIC coplanar lines including conductor-loss effects," *IEEE Trans. Microwave Theory Tech.* **41**(1), 45–52 (1993).
15. M. Casalino et al., "State-of-the-art all-silicon sub-bandgap photodetectors at telecom and datacom wavelengths," *Laser Photonics Rev.* **10**(6), 895–921 (2016).
16. M. Geis et al., "All silicon infrared photodiodes: photo response and effects of processing temperature," *Opt. Express* **15**(25), 16886–16895 (2007).

17. V. M. Hietala et al., "Traveling-wave photodetectors for high-power, large-bandwidth applications," *IEEE Trans. Microwave Theory Tech.* **43**(9), 2291–2298 (1995).
18. R. Ding et al., "Design and characterization of a 30-GHz bandwidth low-power silicon traveling-wave modulator," *Opt. Commun.* **321**, 124–133 (2014).

Ming-Chang M. Lee received his PhD in electrical engineering from the University of California at Los Angeles in 2005. After that, he joined the faculty of the Institute of Photonics Technologies and Department of Electrical Engineering in National Tsing Hua University (NTHU) until the present. His research interests include photonic MEMS, linear and nonlinear silicon photonics, high-speed Group IV optoelectronics, nanophotonics, optomechanics, and microfludic photonics. He is a senior member of IEEE.

Biographies of the other authors are not available.